

Chip-scale optics for balanced polarimetry in atomic magnetometry

Xuting Yang^{1,2}, Meryem Benelajla^{1,2}, and Jennifer T. Choy¹

¹University of Wisconsin – Madison, Madison, Wisconsin 53706 USA

²These authors contributed equally to this work.

Please send correspondences to jennifer.choy@wisc.edu

Abstract

Atomic magnetometry is one of the most sensitive field-measurement techniques for biological, geo-surveying, and navigation applications. An essential process in atomic magnetometry is measurement of optical polarization rotation of a near-resonant beam due to its interaction with atomic spins under an external magnetic field. In this work, we present the design and analysis of a silicon-metasurface-based polarization beam splitter that have been tailored for operation in a rubidium magnetometer. The metasurface polarization beam splitter operates at a wavelength of 795 nm and has a transmission efficiency $> 83\%$ and a polarization extinction ratio > 100 . We show that these performance specifications are compatible with magnetometer operation in miniaturized vapor cells with subpicotesla-level sensitivity and discuss the prospect of realizing compact, high-sensitivity atomic magnetometers with nanophotonic component integration.

Keywords: dielectric metasurface; atomic magnetometry; quantum sensing

1. Introduction

Atomic magnetometers based on optical pumping can provide sub-femtotesla-level sensitivity [1] and are therefore attractive for a host of magnetometry applications including biological sensing [2,3], geo-surveying [4], and magnetic map-based navigation [4,5]. Optically pumped magnetometers (OPMs) typically involve optical pumping of alkali atoms (most commonly rubidium or cesium) with a circularly polarized beam to modify the atomic-spin-dependent optical properties of a medium inside a vapor cell. A linearly polarized probe beam is then used to detect the precession of the atomic spin in the presence of a magnetic field [6]. Typically, this precession causes a polarization rotation of the probe beam which is detected with an optical polarimeter involving a balanced polarimetry, photoelastic or Faraday modulation method [7]. Most OPMs have been realized using an orthogonal pump-probe arrangement with balanced optical polarimetry, since it has a simple configuration and if sufficiently balanced, can suppress common-mode noise arising from laser intensity fluctuations [8].

While breakthroughs in microfabricated vapor cells [9] have enabled the miniaturization of OPMs and their integration with chip-scale photonic technologies such as VCSELs [2,10], state-of-the-art OPMs based on balanced polarimetry detection mostly utilize bulk birefringent polarization optics such as waveplates and polarizing beam splitters which still limit the sensor volume,

scalability, and their use in many portable applications [11–13]. More recently, various schemes have been proposed [14,15] and experimentally demonstrated [16,17] to further integrate OPMs with nanophotonic components, but the performance limits of nanophotonic-integrated OPMs are still being explored.

A common approach to simplify OPM designs and make them more scalable towards realizing multi-channel OPM arrays is to have the pump and probe beams share a single optical axis. These inline OPM schemes can be achieved by using a single elliptically polarized beam [18] or by overlapping the pump and probe beams at different transitions (e.g., the D1 and D2 lines) [19]. Inline OPM configurations are also highly compatible with miniaturized magnetometers since microfabricated vapor cells usually allow only one optical access path.

In this work, we propose integration of inline OPMs with metasurface-based polarization components (Fig. 1a). Specifically, we have designed an efficient and compact balanced polarimetry scheme using a metasurface-based polarization beam splitter (PBS) as depicted in Fig. 1b-c. The geometry of our metasurface-based PBS can be freely optimized and tailored for integration with other atomic species and single-beam OPM designs. In addition, with advances in MEMS vapor cell fabrication [20], it should be possible to directly fabricate metasurfaces on the glass windows of atomic-vapor cells.

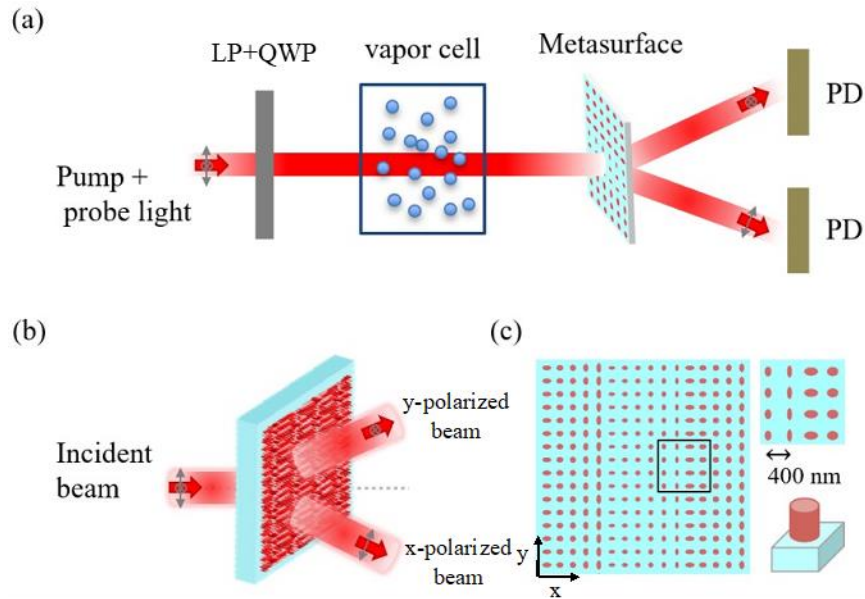


FIG. 1. Our proposed nanophotonic-integrated atomic magnetometer with a metasurface-based polarimeter. (a) Diagrammatic representation of our design. LP: linear polarizer; QWP: quarter waveplate; PD: photodetector (b) Schematic of the metasurface polarizing beam splitter, in which an incident beam splits into beams of orthogonal x and y polarizations. (c) Top view of the proposed metasurface design, which consists of an array of elliptical posts in silicon on a transparent substrate (comprising of quartz or sapphire). The lattice constant and post height are 400 nm and 500 nm respectively.

We then evaluate the accuracy and sensitivity of atomic magnetometry using the miniaturized balanced detection scheme. For our OPM platform, we use Spin Exchange Relaxation Free (SERF) magnetometry in rubidium (Rb) with elliptically polarized light [16]. SERF magnetometers typically operate in a high atomic density regime ($>10^{13} \text{ cm}^{-3}$) where the spin-exchange collision rate of the alkali metal atoms is much larger than the Larmor precession frequency, resulting in longer ground state Zeeman coherence time and thus extremely high sensitivity [18]. In this case, the circularly polarized component of the elliptically polarized light induces atomic polarization in the ground state of isotopically purified Rb atoms through optical pumping. A balanced polarimetry scheme is then used to measure the optical rotation of the linearly polarized component of the transmitted light at the output of the cell. The balanced polarimeter consists of a metasurface PBS that splits the horizontal and vertical linear polarization components of the light beam propagating through the vapor cell medium which are then measured using two independent photodetectors. The detection of the difference of the horizontal and vertical linear polarization intensities provides a direct measure of the optical rotation. The sensitivity of the magnetometer is determined by the signal-to-noise ratio with which the rotation signal is measured.

The paper is structured as follows. In section 2, we introduce our approach to design nanophotonic components for miniaturized balanced detection scheme in in-line OPMs. Optical performance of those components is discussed including transmission losses and polarization extinction ratio. A performance analysis of SERF with metasurface optics is presented in section 3.

2. Design and modeling of metasurface-based PBS

2.1 Design approach

Recently, dielectric metasurfaces made of arrays of elliptical posts have been adopted to design a wide range of nanophotonic components (such as beam splitters, waveplates and optical lenses) offering efficient control of the amplitude, phase, and polarization of light. The majority efforts have been dedicated to engineer metalenses [22], beam shaping devices [23,24], polarization optics [25] and holograms [26]. These advances are beginning to be applied to enhance and miniaturize quantum technologies [16,17,27–29]. In this paper, we adapt an approach to design metasurface polarization components for operation at near-infrared (780 - 795 nm) wavelengths and thus compatible with Rb-based sensors. Our designs maintain high-transmission efficiency and polarization extinction ratio. Our approach is based on the formalism described by Arbabi et al in [25]. Specifically, we implement metasurface optical components by arrays of elliptical posts with the same height, but different diameters to locally modify the phase distribution and polarization of any arbitrary input beam.

We consider a transmissive metasurface polarizing beam splitter design (Fig. 2b) that can be used in a variety of miniaturized OPMs for balanced polarimetry of the magnetometry signal resulting from the polarization rotation of the probe light. For such a metasurface design, the optical

response is fully determined by the phase and amplitude of light in transmission. Fig. 2 (a) shows a schematic illustration of the unit cell structure of the metasurface, consisting of an elliptical post of height H and post diameters r_x and r_y along the x and y axes. In the design, H is fixed while r_x and r_y are tailored to achieve the desired φ_x and φ_y phase shifts for x and y -polarized waves, respectively. To implement beam splitting based on input polarization of a normally incident beam, the desired phase shifts are set to $\varphi_x = -kx\sin\theta$ for an x -polarized beam and $\varphi_y = ky\sin\theta$ for a y -polarized beam, where the wavenumber is $k = 2\pi/\lambda$ and 2θ is the separation angle between the split beams. For this design, the phase shifts are invariant along y .

Next, we construct the metasurface by sampling the phase profile using a square lattice of silicon elliptical posts of various diameters that implement the required phase shift at that position. As stated in [25], to avoid non-zero order diffraction and to achieve a better approximation of the phase profile, the sampling lattice constant a should be smaller than the operating wavelength. In our case, we choose $a = 400 \text{ nm}$ for the Rb D1-line (795 nm).

By varying the geometric parameters r_x, r_y of the elliptical posts, we can impose independent phase shifts along the x and y polarization axes. Figs. 2c and d show the simulated transmission coefficients of an array of elliptical posts with different axis radii from 40 nm to 140 nm for an incident linearly polarized (x or y) plane wave. We see directly from the figure that this platform

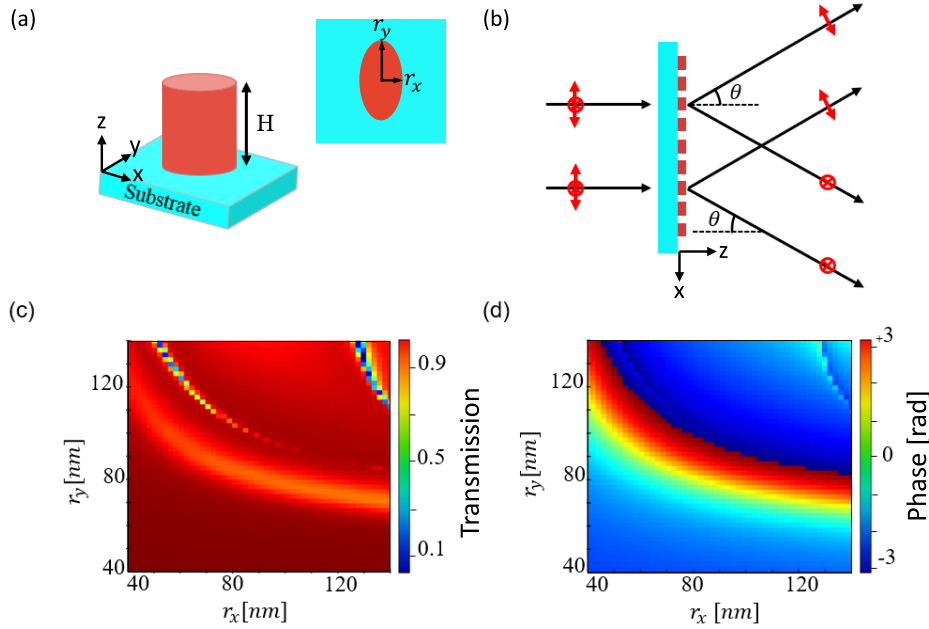


FIG. 2. (a) Geometric illustration of a unit cell with an elliptical cross-section (principal axis lengths r_x and r_y) and height H . (b) Diagrammatic representation for a metasurface polarizing beam splitter, in which the device directs the beam to the left or the right for an x - or y - polarized incident beam. (c)-(d) Calculated transmission and phase shift of an incident x - or y - polarized plane wave, based on full-wave simulation of swept elliptical parameters with fixed lattice constant ($a = 400 \text{ nm}$) and post height ($H = 500 \text{ nm}$).

provides a complete phase coverage independently over φ_x and φ_y while maintaining a relatively high transmission amplitude of $> 87\%$. Elliptical posts of specific radius are selected to match the metasurface phase profile at their position by minimizing the squared error $\varepsilon = |t_x - e^{i\varphi_x}|^2 + |t_y - e^{i\varphi_y}|^2$, where t_i is the transmission coefficient of the elliptical post and φ_i is the calculated phase profile for polarization $i = x, y$, respectively. The resulting metasurface consists of 2500×2500 posts (a portion of which is shown in Fig. 1c) and is designed to achieve a $2\theta = 20^\circ$ split angle between the x and y polarization components. For this design, the maximum ε obtained is 0.0886 while the average ε is 0.0166. These ε values are limited by the mismatch between the desired phase and amplitude profiles and the discretized values in Figs. 2c and 2d, but are nonetheless sufficiently low to ensure good beam splitting performance while maintaining high transmission, as will be shown in the next section.

2.2 Simulated optical performance

To characterize the optical performance of our metasurface beam splitter, we performed finite-difference time domain (FDTD) simulation for a design with a device area of $16 \mu\text{m} \times 16 \mu\text{m}$ using a Gaussian beam source (see Supplementary Information S1 on justification of our simulated beam source). Our design can be extended to a much larger ($>1 \text{ mm}^2$) device footprint, but this representative simulation area is chosen to limit computational time. The incident beam of wavelength $\lambda = 795 \text{ nm}$ (D1 transition of ^{87}Rb) is propagating in the z -direction at normal incidence. We evaluated the transmission characteristics of the metasurface for different input polarization angles. Fig. 3a represents the normalized transmitted far-field intensity for an incident linear polarization at 45° (comprising of an equal superposition of x and y polarizations). As expected, the designed metasurface splits the 45° linearly polarized incident beam into x - and y -

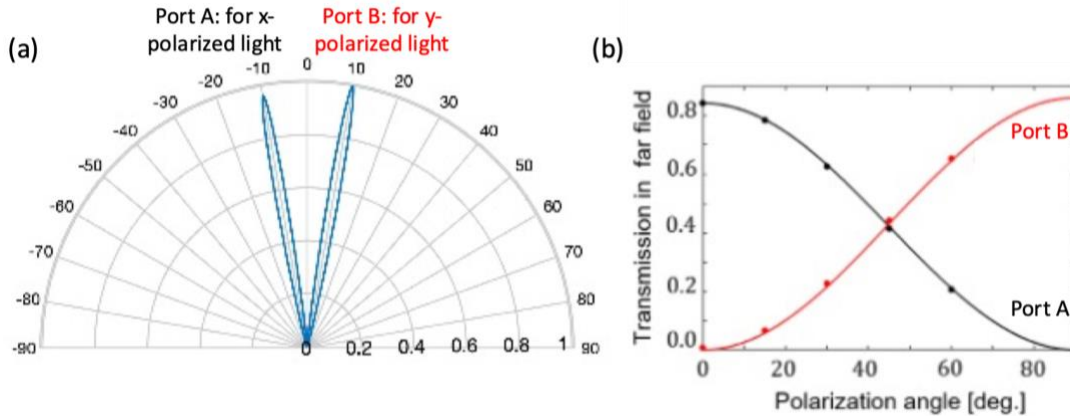


FIG. 3. (a) The 3D far-field scattering patterns for the 45° -linearly polarized incident Gaussian beam under normal incidence. (b) The normalized transmission in far field for different polarization angles of the input beam. Each data point for the x and y -polarized beam is obtained by integrating the optical power within their respective scattered spot, then normalize it to the overall transmission power. The solid lines indicate sinusoidal fit to the data.

polarized beams propagated along different directions. The split beams have a slightly different transmittance with a split ratio of 49% and 47% for x and y polarization respectively. The transmittance among various input polarization angles is shown in Fig.3(b). The results for x -polarized beam (respectively for y -polarized beam) demonstrate that the transmitted intensity varies as the square of the cosine (respectively sine) of the polarization angle of the input beam. This is in good consistency with Malus law for linear polarizers.

The performance shown here is for input beams of wavelength $\lambda = 795 \text{ nm}$ at normal incidence, in which the simulated transmittance is over 80% exhibits a slight linear dichroism (83.3% for x -polarized beam and 85.8% for y -polarized beam). Polarization extinction ratio (PER) is another important performance metric for PBS devices. We define the PER for each output port as the light intensity of main polarization mode divided by the light intensity of the orthogonal polarization mode (see Supplementary Information S2). For normal incidence, the PER is 113.4 for x polarization and 675.7 for y polarization.

In reality, the transmission efficiency of the metasurface structure may vary with the incident angle and the wavelength as it has been reported in earlier works [15]. These deviations are significant considerations in an OPM, which may have axial misalignments between an input beam and the atomic cell and sometimes rely on multi-wavelength (e.g., D1 and D2 lines of Rb transitions) pump and probe beams. In what follows, we analyze the transmission and polarization extinction of our design for different angles of incidence and wavelengths to evaluate the nanophotonic requirements for achieving sensitive balanced polarimetry measurements.

Figs. 4a and 4b show the simulated transmittance and polarization extinction ratio as a function of incident wavelength between 700 and 820 nm for the x and y polarizations. For both polarizations, the transmittance of the metasurface PBS goes up from around 60% to more than 80%, which is expected since the absorption loss in silicon decreases as the incident wavelength approaches the band gap (around 1.12 eV or 1.1 μm for single-crystalline silicon). The polarization extinction ratio peaks at the designed wavelength (795 nm) with significant deterioration at shorter wavelengths due to the emergence of higher diffraction orders.

Figs. 4c and 4d show the transmittance and polarization extinction ratio at different incident angles from 0 to 10°. Both performance metrics suffer from degradation as the incident angle exceeds 5°, which is again attributed to the higher-order diffraction as the incidence condition deviates from the requirement for zero-order diffraction: $\lambda \gg \frac{a}{\cos\theta}$ (where θ is the incident angle). Nevertheless, the polarization extinction ratio maintains a level of > 100 over a range of 10°, an alignment condition that can be readily achieved in the actual experiment.

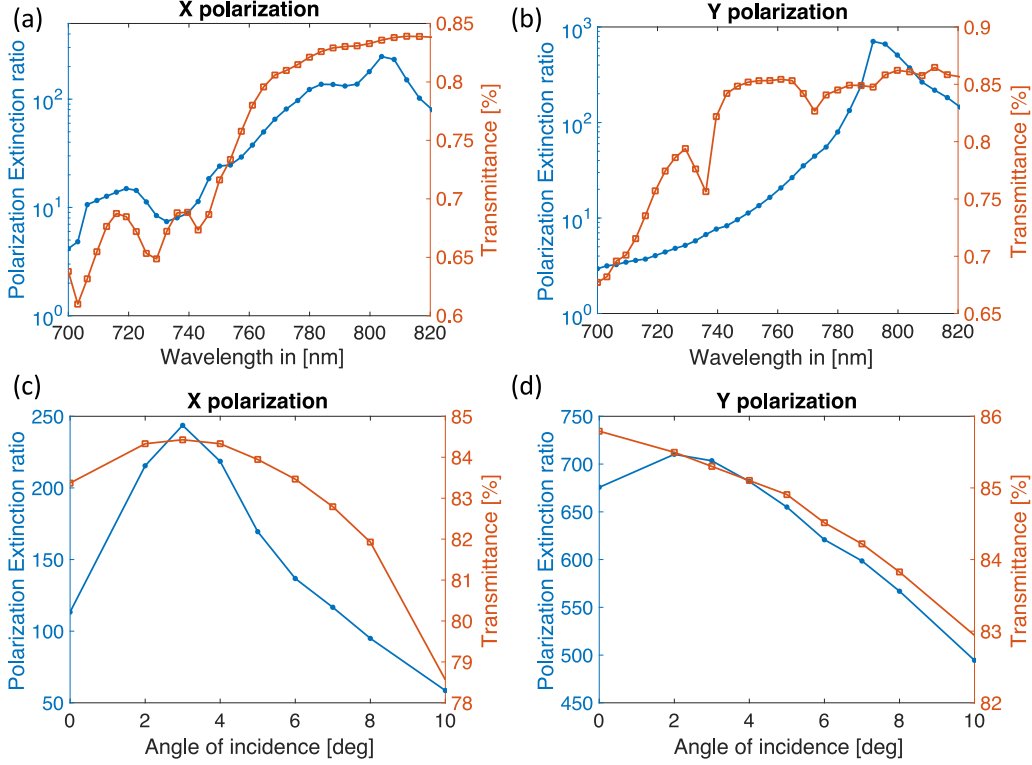


FIG. 4. Simulated intensity transmission and polarization extinction ratio as a function of incident light wavelength for (a) x -polarized beam and (b) y -polarized beam and as function of the incident angle for (c) x -polarized beam and (d) y -polarized beam.

3. Sensitivity performance analysis

In this section, we evaluate how the optical performance of our proposed metasurface PBS affects balanced polarimetry and thereby the sensitivity and accuracy of an OPM. Our PBS design can be compatible with millimeter-scale, microfabricated Rb cells involving separate non-parallel [15] or inline pump and probe beams. For reasons specified in Section 1, we focus on the magnetometry schemes that are compatible with inline pump-probe configurations such as the Mx [30], Bell-Bloom [31], SERF [32], and nonlinear magneto-optical rotation (NMOR) [33] OPMs. Of the above schemes proposed, SERF is an attractive candidate since it provides the highest sensitivities among OPMs and has been demonstrated to achieve sub-picotesla sensitivity in microfabricated cells [32]. Moreover, while the shot-noise-limited sensitivity of SERF magnetometry is expected to degrade with decreasing cell size [34], SERF operation relies on a high buffer gas pressure which is also necessary in very small ($\lesssim \text{mm}^3$) vapor cells to prevent decoherence from collisions of the atoms with the cell wall. A high buffer gas pressure would broaden atomic transitions and preclude the operation of NMOR [35]. Finally, SERF using elliptically polarized light has shown very promising results with device scale down to 5 mm [16, 31] and can require only a single optical beam to operate [18,19], and thus highly compatible with nanophotonic integration.

We thus choose SERF magnetometry using a single elliptical beam as the platform for evaluating the sensitivity of a metasurface-integrated magnetometer [18]. In this scheme, an elliptically polarized light close to the ^{87}Rb D1 transition interacts with a ^{87}Rb vapor cell of optical path length l and Rb number density n to generate atomic spin polarization. This same optical beam is used to detect spin polarization via balanced polarimetry. An amplitude-modulating field is applied along the direction of magnetic field measurement (along x) which must be transverse to the light propagation direction; all other field components are nulled. The optical signal is then detected using lock-in detection at the modulation frequency (ω_{mod}). The theory of operation for SERF magnetometry with elliptical light was worked out in [18] for the case of an ideal PBS with transmittance $T = 1$ and infinite polarization extinction ratio. In this scenario, the balanced polarimetry gives the polarization angle rotation ϕ via the differential signal of the two outputs from the PBS:

$$\mathcal{D} = E_0^2 e^{-\sigma n l} \cos 2\beta \sin \phi \quad (1)$$

where ϕ is proportional to the spin polarization along the optical axis (see Supplementary Information S3 for derivation); E_0 is the electric field amplitude; $e^{-\sigma n l}$ is related to light absorption by Rb atoms (whereby σ is the photon absorption cross section for unpolarized Rb atoms); β is the ellipticity of the light and is set to $\pi/8$ [18]. In the low polarization limit, the signal \mathcal{D} is linear in terms of spin polarization P_z . This optical rotation will allow us to determine the transverse magnetic field.

Note that the differential signal \mathcal{D} only includes the polarization rotation term induced by circular birefringence. Such simplicity cannot be assumed for our metasurface PBS which has a non-negligible transmittance difference for the two orthogonal linear polarization and polarization leakage. We thus modify the theory to incorporate these non-idealities. Let T_x, T_y be the transmittance for the x and y polarizations, b_x and b_y be the percentage of the transmitted optical power that is leaked into the other output of the PBS for a pure x and y polarization input, respectively. b is related to PER through $b = \frac{1}{PER+1}$. Then the outputs of the PBS become:

$$\begin{aligned} I_x &= T_x(1 - b_x)I_{x,in} + T_y b_y I_{y,in} \\ I_y &= T_x b_x I_{x,in} + T_y(1 - b_y)I_{y,in} \end{aligned} \quad (2)$$

i.e. the two outputs are now a linear superposition of the light intensities along two orthogonal polarization axes. The direct consequence of this intensity mixture is that the differential signal will now contain an additional term due to circular dichroism that is proportional to σ . It can be shown that under this ‘‘imperfect PBS’’ model, the differential signal can be approximated as (see Supplementary Information S3 for the derivation):

$$\mathcal{D} = E_0^2 e^{-\sigma n l} (\eta \cos 2\beta \sin \phi - \frac{(T_y(1 - 2b_y) - T_x(1 - 2b_x))}{4} \sigma n l \sin 2\beta P_z) \quad (3)$$

where

$$\eta = \frac{T_x(1 - 2b_x) + T_y(1 - 2b_y)}{2} \sqrt{1 - \left(\frac{T_y(1 - 2b_y) - T_x(1 - 2b_x)}{\cos 2\beta (T_x(1 - 2b_x) + T_y(1 - 2b_y))} \right)^2}; \quad (4)$$

ϕ is the polarization rotation angle and is proportional to P_z . We see that the imperfect PBS results in two modifications in the expression of the differential signal: first, the original polarization rotation signal is attenuated by a factor of η ; second, the imperfect PBS introduces another term related to the change of the polarization ellipticity induced by the circular dichroism of the atomic medium, which is also proportional to P_z in the low polarization limit.

We will now benchmark the performance of a metasurface-integrated magnetometer against one based on ideal optics (namely, a PBS with near unity transmittance, ultra-high PER, and no linear dichroism). We use identical excitation and cell conditions as in [18], in which the Rb vapor cell is filled with 300 Torr helium and 100 Torr nitrogen and heated to 200°C. The laser frequency detuning is set to $\nu_0 - \nu = 45 \text{ GHz}$. These conditions lead to a linewidth $\Delta\nu$ of 7.97 GHz, optical pumping rate of 880 Hz, and a spin relaxation rate of 1200 Hz. Fig. 5 shows the differential signal \mathcal{D} as a function of the transverse magnetic field B_x for magnetometers based on ideal optics (red) and our metasurface design (blue) for a vapor cell with $l = 5 \text{ mm}$. We can see from the Fig. 6 that the incorporation of the metasurface PBS into the magnetometer does not change the dispersive character of the signal and only modifies the signal amplitude by a scaling factor ξ that is given by:

$$\xi = \eta - \frac{(T_y(1 - 2b_y) - T_x(1 - 2b_x))}{8} \frac{\Delta\nu}{\nu_0 - \nu} \quad (5)$$

For our design, $\xi \cong 0.836$. This means that the sensitivity of the metasurface-integrated magnetometer is degraded by a factor of 1.2. Our metasurface PBS has a high enough polarization extinction ratio such that $b_x, b_y \ll 1$ with no significant linear dichroism $|T_x - T_y| \ll 1$, and that the laser detuning is sufficiently larger than the pressure-broadened linewidth. In this situation, the signal amplitude is simply attenuated by the mean transmittance of \hat{x} and \hat{y} polarization: $\xi \cong \frac{T_x + T_y}{2}$. Our analysis shows that any polarization splitting device can be suitable for magnetometry with an elliptical input beam as long as the component can be oriented in a way such that its two outputs are balanced with the incident elliptically polarized light, i.e. $|T_y(1 - 2b_y) - T_x(1 - 2b_x)| < \cos 2\beta (T_x(1 - 2b_x) + T_y(1 - 2b_y))$. Even for a “bad” PBS with significant linear dichroism and polarization leakage, it is still possible to get a decent polarimetry signal by

optimizing expression (3) with respect to ellipticity β and laser detuning $\nu_0 - \nu$ (see Supplementary Information S3).

In the future, it may be possible to further improve the metasurface design using adjoint optimization methods [36–38] that minimize the figure of merit (FOM) defined as $FOM = \left| \frac{T_y(1-2b_y) - T_x(1-2b_x)}{T_x(1-2b_x) + T_y(1-2b_y)} \right|$. This analysis can also serve as a useful guideline for designing nanophotonic components for other quantum sensors.

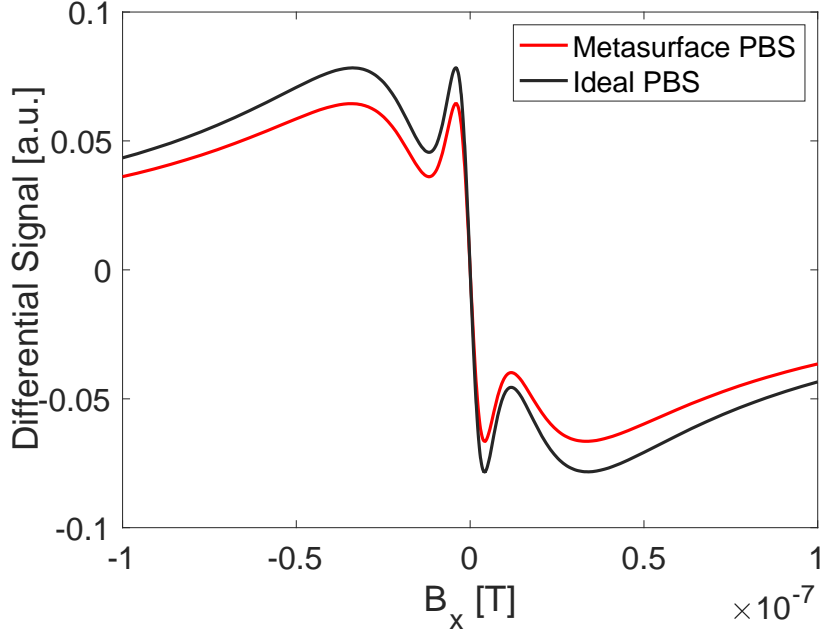


FIG. 5. Simulated differential signal \mathcal{D} with lock-in detection at the modulating frequency ω_{mod} as a function of B_x with an ideal PBS (red) and metasurface PBS (blue).

4. Conclusion and outlook

We have demonstrated a metasurface-based balanced polarimeter design for a compact Rb magnetometer based on SERF and have connected its optical performance to the magnetometer accuracy and sensitivity. This design can be realized with electron-beam lithography and reactive-ion etching techniques on single-crystal silicon films grown on transparent substrates. It may be possible to incorporate the metasurface PBS as part of the glass wafer anodically bonded to the silicon housing during MEMS fabrication of mm-scale vapor cells [10]. Modeling of balanced polarimetry using simulated transmittance and PER shows that the nanophotonic component can be integrated into SERF magnetometry with only a 20% degradation in sensitivity. Our analysis of the magnetometry dependence of an imperfect PBS may inform future efforts to design and integrate nanophotonic polarization optics into atomic magnetometers and other atom-based sensors.

Acknowledgments

This work is supported by the Office of Naval Research under Grant No. N00014-20-1-2598 and the Wisconsin Alumni Research Foundation. The authors thank Mikhail Kats and Thad Walker for helpful discussions on the metasurface design and its suitability to atomic magnetometry platforms.

Disclosures The authors declare no conflicts of interest.

Data availability Data underlying the results presented in this paper are not publicly available at this time but may be obtained from the authors upon request.

Supplemental document See Supplementary Information.

References

1. I. K. Kominis, T. W. Kornack, J. C. Allred, and M. V. Romalis, "A subfemtotesla multichannel atomic magnetometer," *Nature* **422**(6932), 596–599 (2003).
2. S. Knappe, T. H. Sander, O. Kosch, F. Wiekhorst, J. Kitching, and L. Trahms, "Cross-validation of microfabricated atomic magnetometers with superconducting quantum interference devices for biomagnetic applications," *Appl. Phys. Lett.* **97**(13), 133703 (2010).
3. C. N. Johnson, P. D. D. Schwindt, and M. Weisend, "Multi-sensor magnetoencephalography with atomic magnetometers," *Phys. Med. Biol.* **58**(17), 6065–6077 (2013).
4. M. Purucker, B. Langlais, N. Olsen, G. Hulot, and M. Manda, "The southern edge of cratonic North America: Evidence from new satellite magnetometer observations," *Geophysical Research Letters* **29**(15), 56-1-56-4 (2002).
5. C. Tyren, "Magnetic terrain navigation," in *Proceedings of the 1987 5th International Symposium on Unmanned Untethered Submersible Technology* (1987), **5**, pp. 245–256.
6. D. Budker and M. Romalis, "Optical magnetometry," *Nature Phys* **3**(4), 227–234 (2007).
7. S. J. Seltzer, "Developments in alkali -metal atomic magnetometry," Ph.D., Princeton University (n.d.).
8. D. Hunter, S. Piccolomo, J. D. Pritchard, N. L. Brockie, T. E. Dyer, and E. Riis, "Free-Induction-Decay Magnetometer Based on a Microfabricated Cs Vapor Cell," *Phys. Rev. Applied* **10**(1), 014002 (2018).
9. W. C. Griffith, S. Knappe, and J. Kitching, "Femtotesla atomic magnetometry in a microfabricated vapor cell," *Opt. Express* **18**(26), 27167–27172 (2010).
10. P. D. D. Schwindt, S. Knappe, V. Shah, L. Hollberg, J. Kitching, L.-A. Liew, and J. Moreland, "Chip-scale atomic magnetometer," *Appl. Phys. Lett.* **85**(26), 6409–6411 (2004).
11. Y. Xuan, R. Sengupta, and Y. Fallah, "Making indoor maps with portable accelerometer and magnetometer," in *2010 Ubiquitous Positioning Indoor Navigation and Location Based Service* (2010), pp. 1–7.
12. J. F. D. F. Araujo, M. C. Costa, S. R. W. Louro, and A. C. Bruno, "A portable Hall magnetometer probe for characterization of magnetic iron oxide nanoparticles," *Journal of Magnetism and Magnetic Materials* **426**, 159–162 (2017).
13. S. Filice, R. Rossi, and G. Crisi, "Assessment of movement-induced time-varying magnetic fields exposure in magnetic resonance imaging by a commercial portable magnetometer," *Radiation Protection Dosimetry* **185**(3), 326–330 (2019).

14. J. Hu, J. Lu, Z. Liang, L. Liu, W. Wang, P. Zhou, and M. Ye, "Integrated Polarization-Splitting Grating Coupler for Chip-Scale Atomic Magnetometer," *Biosensors* **12**(7), 529 (2022).
15. Z. Liang, B. Zhou, J. Lu, Y. Liu, J. Hu, P. Zhou, W. Wang, L. Liu, G. Hu, and M. Ye, "Metasurface enabled on-chip double-beam scheme for SERF atomic magnetometer," *Optics Communications* **525**, 128850 (2022).
16. Y. Sebbag, A. Naiman, E. Talker, Y. Barash, and U. Levy, "Chip-Scale Integration of Nanophotonic-Atomic Magnetic Sensors," *ACS Photonics* **8**(1), 142–146 (2021).
17. Y. Sebbag, E. Talker, A. Naiman, Y. Barash, and U. Levy, "Demonstration of an integrated nanophotonic chip-scale alkali vapor magnetometer using inverse design," *Light Sci Appl* **10**(1), 54 (2021).
18. V. Shah and M. V. Romalis, "Spin-exchange relaxation-free magnetometry using elliptically polarized light," *Phys. Rev. A* **80**(1), 013416 (2009).
19. C. Johnson, P. D. D. Schwindt, and M. Weisend, "Magnetoencephalography with a two-color pump-probe, fiber-coupled atomic magnetometer," *Appl. Phys. Lett.* **97**(24), 243703 (2010).
20. P. Knapkiewicz, "Technological Assessment of MEMS Alkali Vapor Cells for Atomic References," *Micromachines* **10**(1), 25 (2019).
21. S. I. Kanorsky, A. Weis, J. Wurster, and T. W. Hänsch, "Quantitative investigation of the resonant nonlinear Faraday effect under conditions of optical hyperfine pumping," *Phys. Rev. A* **47**(2), 1220–1226 (1993).
22. M. Khorasaninejad, W. T. Chen, R. C. Devlin, J. Oh, A. Y. Zhu, and F. Capasso, "Metalenses at visible wavelengths: Diffraction-limited focusing and subwavelength resolution imaging," *Science* **352**(6290), 1190–1194 (2016).
23. D. Lin, P. Fan, E. Hasman, and M. L. Brongersma, "Dielectric gradient metasurface optical elements," *Science* **345**(6194), 298–302 (2014).
24. A. Arbabi, Y. Horie, A. J. Ball, M. Bagheri, and A. Faraon, "Subwavelength-thick lenses with high numerical apertures and large efficiency based on high-contrast transmitarrays," *Nat Commun* **6**(1), 7069 (2015).
25. A. Arbabi, Y. Horie, M. Bagheri, and A. Faraon, "Dielectric metasurfaces for complete control of phase and polarization with subwavelength spatial resolution and high transmission," *Nature Nanotech* **10**(11), 937–943 (2015).
26. L. Wang, S. Kruk, H. Tang, T. Li, I. Kravchenko, D. N. Neshev, and Y. S. Kivshar, "Grayscale transparent metasurface holograms," *Optica*, *OPTICA* **3**(12), 1504–1505 (2016).
27. K. Gallacher, P. F. Griffin, E. Riis, M. Sorel, and D. J. Paul, "Silicon nitride waveguide polarization rotator and polarization beam splitter for chip-scale atomic systems," *APL Photonics* **7**(4), 046101 (2022).
28. R. Zektzer, N. Mazurski, Y. Barash, and U. Levy, "Nanoscale atomic suspended waveguides for improved vapour coherence times and optical frequency referencing," *Nat. Photon.* **15**(10), 772–779 (2021).
29. L. Zhu, X. Liu, B. Sain, M. Wang, C. Schlickriede, Y. Tang, J. Deng, K. Li, J. Yang, M. Holynski, S. Zhang, T. Zentgraf, K. Bongs, Y.-H. Lien, and G. Li, "A dielectric metasurface optical chip for the generation of cold atoms," *Science Advances* **6**(31), eabb6667 (2020).
30. D. Arnold, S. Siegel, E. Grisanti, J. Wrachtrup, and I. Gerhardt, "A rubidium Mx-magnetometer for measurements on solid state spins," *Review of Scientific Instruments* **88**(2), 023103 (2017).
31. R. Jimenez-Martinez, W. C. Griffith, Y.-J. Wang, S. Knappe, J. Kitching, K. Smith, and M. D. Prouty, "Sensitivity Comparison of Mx and Frequency-Modulated Bell–Bloom Cs

- Magnetometers in a Microfabricated Cell," IEEE Transactions on Instrumentation and Measurement **59**(2), 372–378 (2010).
32. V. Shah, S. Knappe, P. D. D. Schwindt, and J. Kitching, "Subpicotesla atomic magnetometry with a microfabricated vapour cell," Nature Photon **1**(11), 649–652 (2007).
 33. D. Budker, D. F. Kimball, V. V. Yashchuk, and M. Zolotarev, "Nonlinear magneto-optical rotation with frequency-modulated light," Phys. Rev. A **65**(5), 055403 (2002).
 34. J. C. Allred, R. N. Lyman, T. W. Kornack, and M. V. Romalis, "High-Sensitivity Atomic Magnetometer Unaffected by Spin-Exchange Relaxation," Phys. Rev. Lett. **89**(13), 130801 (2002).
 35. Defense Technical Information Center, *DTIC ADA544874: Development of a Micro-Fabricated Total-Field Magnetometer* (2011).
 36. C. M. Lalau-Keraly, S. Bhargava, O. D. Miller, and E. Yablonovitch, "Adjoint shape optimization applied to electromagnetic design," Opt. Express, OE **21**(18), 21693–21701 (2013).
 37. M. Mansouree, A. McClung, S. Samudrala, and A. Arbabi, "Large-Scale Parametrized Metasurface Design Using Adjoint Optimization," ACS Photonics **8**(2), 455–463 (2021).
 38. R. A. Wambold, Z. Yu, Y. Xiao, B. Bachman, G. Jaffe, S. Kolkowitz, J. T. Choy, M. A. Eriksson, R. J. Hamers, and M. A. Kats, "Adjoint-optimized nanoscale light extractor for nitrogen-vacancy centers in diamond," Nanophotonics **10**(1), 393–401 (2021).

Supplementary Information for “Chip-scale optics for balanced polarimetry in atomic magnetometry”

Xuting Yang^{1,2}, Meryem Benelajla^{1,2}, and Jennifer T. Choy^{1,*}

¹University of Wisconsin – Madison, Madison, Wisconsin 53706 USA

²These authors contributed equally to this work.

S1: Plane-wave approximation

Here we justify our assumption that the phase profile $\varphi(x, y)$ of our metasurface polarizing beamsplitter that is designed for a normal plane wave incidence would still apply to the case where the incident beam has a Gaussian profile. Let us consider a Gaussian source polarized along the x direction:

$$U(x, y, z) = E_0 \hat{x} \frac{w_0}{w(z)} \exp\left(-\frac{x^2 + y^2}{w(z)^2}\right) \exp\left(-i\left(kz + k \frac{x^2 + y^2}{2R(z)} - \psi(z)\right)\right) \quad (\text{Eq. S1})$$

where w_0 is the waist radius, $w(z) = w_0 \sqrt{1 + \left(\frac{\lambda z}{\pi w_0^2}\right)^2}$ is the radius at which the field amplitudes decay to $\frac{1}{e}$ of their axial values, $R(z) = \frac{z^2 + \left(\frac{\pi w_0^2}{\lambda}\right)^2}{z}$ is the radius of curvature, $\psi(z) = \arctan\left(\frac{\lambda z}{\pi w_0^2}\right)$ is the Gouy phase.

Our main argument here is that $U(x, y, z)$ is a solution to the paraxial Helmholtz equation, and can thus be well-approximated by a normal incident plane wave plus a small component of paraxial wave:

$$\begin{aligned} U(x, y, z) &= \iint u(k_x, k_y) e^{-i(k_x x + k_y y + k_z z)} dk_x dk_y \\ &= \iint e^{-ikz} u(k_x, k_y) e^{-i\left(k_x x + k_y y - \frac{1}{2k}(k_x^2 + k_y^2)z\right)} dk_x dk_y \end{aligned} \quad (\text{Eq. S2})$$

where we have used the fact that $k_x, k_y \ll k_z$.

We claim that the elliptical posts will impose the same phase shift $\varphi(x, y) = \mp k_x x \sin\Theta$ for a paraxial plane wave, so that the gaussian source after transmitting through the metasurface will become:

$$U'(x, y, z) = \iint e^{-ik(z \mp x \sin\Theta)} u(k_x, k_y) e^{-i\left(k_x x + k_y y - \frac{1}{2k}(k_x^2 + k_y^2)z\right)} dk_x dk_y$$

which is just the gaussian beam deflected by angle $\mp\Theta$. In what follows, we justify our claim. Let us quantify this argument by calculating the Fourier component $u(\theta)$ of a Gaussian beam, where θ indicates the angle between the wavevector and the propagation direction \hat{z} . We write the k -vector in spherical basis: $k_x = K \sin\theta \cos\varphi$, $k_y = K \sin\theta \sin\varphi$, $k_z = K \cos\theta$. Here φ is the azimuth angle.

$$\begin{aligned}
u(K, \theta) &= \iiint U(x, y, z) e^{i(k_x x + k_y y + k_z z)} dx dy dz \\
&= E_0 w_0 \int_{-\infty}^{+\infty} \frac{1}{w(z)} e^{i(K \cos \theta - k)z + \psi(z)} dz \\
&\quad \times \iint e^{-\frac{x^2 + y^2}{w(z)^2}} e^{i(K \sin \theta \sin \phi x + K \sin \theta \sin \phi y - k \frac{x^2 + y^2}{2R(z)})} dx dy
\end{aligned} \tag{Eq. S3}$$

It can be proven that

$$|u(K, \theta)| = C(w_0, \lambda, E_0) |g(z,)| e^{-\frac{K^2 w_0^2}{4} \sin^2 \theta} \tag{Eq. S4}$$

Here $C(w_0, \lambda, E_0)$ is a constant that only depends on the incident Gaussian beam parameters. $g = \int_{-\infty}^{+\infty} \frac{e^{i(K \cos \theta - k)z + \psi(z)}}{\sqrt{1 + (\frac{\lambda z}{\pi w_0^2})^2}} dz$ is a complex function of θ .

If $\alpha = K \cos \theta - k \neq 0$, then $g(\alpha) = \int_{-\infty}^{+\infty} \frac{e^{i(\alpha z + \psi(z))}}{\sqrt{1 + (\frac{\lambda z}{\pi w_0^2})^2}} dz$ converges, therefore the Fourier components that matter are the ones with $K = \frac{k}{\cos \theta}$. We now have:

$$|u(\theta)| \propto e^{-\frac{k^2 w_0^2}{4} \tan^2 \theta} \tag{Eq. S5}$$

The angular dependence of the Fourier component decays very fast with respect to θ . We define a cutoff angle θ_0 where its corresponding Fourier coefficient is only $e^{-4} \approx 1.8\%$ of that of the normal component. Then:

$$\theta_0 = \arctan\left(\frac{4}{k w_0}\right) \tag{Eq. S6}$$

For our simulation, $w_0 = 4 \mu m$ and $k = 7.9 \times 10^6 m^{-1}$, the cutoff angle $\theta_0 = 7^\circ$. For a realistic beam size $w_0 = 1 mm$ in the magnetometer experiment, $\theta_0 = 0.03^\circ$. It follows that the Gaussian source in the actual experiment is very well approximated by a normal incident plane wave. Indeed, simulated phase shift of a 795-nm plane wave with incident angle at the cutoff angle $\theta_0 = 0.03^\circ$ shows less than 10^{-6} deviation from that for a normally incident plane wave.

S2: Determination of transmittance and polarization extinction ratio

In this section we describe our method for calculating the transmittance T and the polarization extinction ratio (PER) of the metasurface PBS. The transmittance T_0 from the transmission of the field through the metasurface is first extracted from a field monitor placed a few wavelengths away from the metasurface. In the far-field projection, the transmitted field intensity $|E|^2$ is integrated at the two PBS outputs whose locations are determined by the splitting angle 2θ . The integration area is determined through the solid angle Ω of the projection hemisphere. We choose $\Omega = 2\pi(1 -$

$\cos 7^\circ$) (half angle 7°) to ensure we have covered most of the scattered light and the two integration areas do not overlap. The reported transmittance values in the main text take into account both the initial transmittance T_0 and the fraction of intensity within the solid angle:

$$T = T_0 \times \frac{\int_{\text{cone}} |E|^2}{\int_{\text{hemisphere}} |E|^2} \quad (\text{Eq. S7})$$

We now define I_{main} to be the integrated intensity in the far field that corresponds to the main polarization mode and I_{leak} to be the intensity corresponding to the orthogonal polarization mode, then the PER is calculated as:

$$PER = \frac{I_{\text{main}}}{I_{\text{leak}}} \quad (\text{Eq. S8})$$

S3: Derivation of differential signal for an imperfect PBS

In this section we show the derivation of the differential signal between the output ports of an imperfect PBS, for SERF magnetometry with a single elliptical beam [1]. We write an electric field with arbitrary polarization and amplitude in the x and y polarization basis: $E = c_1 \hat{x} + c_2 i \hat{y}$ where c_1 and c_2 are complex numbers.

If the optical axes of the PBS are oriented with respect to the $x - y$ coordinate by angle δ , then the two outputs of the metasurface PBS are:

$$\begin{aligned} I_1 &= \mathcal{P}(T_x(1 - b_x)|c_1 \cos \delta + i c_2 \sin \delta|^2 + T_y b_y |-c_1 \sin \delta + i c_2 \cos \delta|^2) \\ I_2 &= \mathcal{P}(T_x b_x |c_1 \cos \delta + i c_2 \sin \delta|^2 + T_y(1 - b_y) |-c_1 \sin \delta + i c_2 \cos \delta|^2) \end{aligned} \quad (\text{Eq. S9})$$

Here \mathcal{P} is some constant is related to vacuum permittivity and detection efficiency. With the differential signal being:

$$\begin{aligned} \mathcal{D} &= I_1 - I_2 \\ &= \mathcal{P}[T_x(1 - 2b_x)|c_1 \cos \delta + i c_2 \sin \delta|^2 - T_y(1 - 2b_y) |-c_1 \sin \delta + i c_2 \cos \delta|^2] \\ &= \mathcal{P}[T_x(1 - 2b_x)(|c_1|^2 \cos^2 \delta + i(\bar{c}_1 c_2 - c_1 \bar{c}_2) \sin \delta \cos \delta + |c_2|^2 \sin^2 \delta) \\ &\quad - T_y(1 - 2b_y)(|c_1|^2 \sin^2 \delta + i(c_1 \bar{c}_2 - \bar{c}_1 c_2) \sin \delta \cos \delta \\ &\quad + |c_2|^2 \cos^2 \delta)] \end{aligned} \quad (\text{Eq. S10})$$

In the absence of an atomic medium, $|c_1|^2 = \cos^2 \theta$, $|c_2|^2 = \sin^2 \theta$, $\bar{c}_1 c_2 - c_1 \bar{c}_2 = 0$. Let $\mathcal{D} = 0$ and we get the expression for δ that balances the two outputs:

$$\tan^2 \delta = \frac{T_x(1 - 2b_x) \cos^2 \beta - T_y(1 - 2b_y) \sin^2 \beta}{T_y(1 - 2b_y) \cos^2 \beta - T_x(1 - 2b_x) \sin^2 \beta} \quad (\text{Eq. S11})$$

The interaction of the field with rubidium atoms causes polarization rotation and ellipticity change, with the coefficients now being:

$$|c_1|^2 = \frac{1}{2} [(e^{-n\sigma l(1+P_z)} + e^{-n\sigma l(1-P_z)}) + (e^{-n\sigma l(1+P_z)} - e^{-n\sigma l(1-P_z)}) \sin 2\beta + 2e^{-n\sigma l} \cos 2\beta \cos \phi] \quad (\text{Eq. S12})$$

$$|c_2|^2 = \frac{1}{2} [(e^{-n\sigma l(1+P_z)} + e^{-n\sigma l(1-P_z)}) + (e^{-n\sigma l(1+P_z)} - e^{-n\sigma l(1-P_z)}) \sin 2\beta - 2e^{-n\sigma l} \cos 2\beta \cos \phi] \quad (\text{Eq. S13})$$

$$\bar{c}_1 c_2 - c_1 \bar{c}_2 = -2ie^{-n\sigma l} \cos 2\beta \sin \phi \quad (\text{Eq. S14})$$

where $\phi = cr_e f n l P_z \text{Re}(L(\nu))$ is the polarization rotation angle defined in [1]. Here c is the speed of light in vacuum; r_e is the classical electron radius; $f \cong \frac{1}{3}$ is the oscillator strength of the rubidium D1 transition; l is the optical path length; n is the Rb number density; P_z is the atomic spin polarization along z direction; $L(\nu) = \frac{1}{\nu_0 - \nu + i\frac{\Delta\nu}{2}}$ is the pressure-broadened Lorentzian profile with a full width at half maximum $\Delta\nu$ centered at ν_0 . Plug in the expressions for c_1, c_2 and δ into expression (Eq. S10), and select \mathcal{P} such that our result reduces to the expression given in [1] when $T_x = T_y = 1, b_x = b_y = 0$, we have:

$$\begin{aligned} \mathcal{D} = & \frac{1}{8} E_0^2 [(T_x(1-2b_x) - T_y(1-2b_y)) \\ & \times (e^{-n\sigma l(1+P_z)} + e^{-n\sigma l(1-P_z)} - \sin 2\beta (e^{-n\sigma l(1+P_z)} - e^{-n\sigma l(1-P_z)})) \\ & + 2(T_y(1-2b_y) - T_x(1-2b_x)) e^{-n\sigma l} \cos \phi \\ & + 4(T_x(1-2b_x) + T_y(1-2b_y)) \\ & \times \sqrt{1 - \left(\frac{T_y(1-2b_y) - T_x(1-2b_x)}{\cos 2\beta (T_x(1-2b_x) + T_y(1-2b_y))} \right)^2} e^{-n\sigma l} \cos 2\beta \sin \phi] \end{aligned} \quad (\text{Eq. S15})$$

Expanding and keep the first order of P_z , we have:

$$\begin{aligned} \mathcal{D} = & E_0^2 e^{-\sigma n l} \left(\frac{T_x(1-2b_x) + T_y(1-2b_y)}{2} \right. \\ & \times \sqrt{1 - \left(\frac{T_y(1-2b_y) - T_x(1-2b_x)}{\cos 2\beta (T_x(1-2b_x) + T_y(1-2b_y))} \right)^2} \cos 2\beta \sin \phi \\ & \left. - \frac{(T_y(1-2b_y) - T_x(1-2b_x))}{4} \sigma n l \sin 2\beta P_z \right) \end{aligned} \quad (\text{Eq. S16})$$

For $\phi, \sigma n l P_z \ll 1$, \mathcal{D} reduces to

$$\mathcal{D} = \mathcal{D} = \xi E_0^2 e^{-\sigma n l} \cos 2\beta \sin \phi \quad (\text{Eq. S17})$$

where ξ is defined in main text expression (5).

Let us now discuss what conditions should the transmittance and PER of the PBS satisfy to generate a dispersive signal with discernible amplitude. Note that under the SERF condition, the

atomic vapor is usually dense enough that the modification of the optical absorption due to spin polarization $\Lambda = n\sigma l P_z$ is no longer small enough for the first order approximation to remain valid (except for sufficiently small vapor cells, see Fig. S1). Therefore, the polarimetry signal from circular dichroism (which is the one related to $Im(L(\nu))$) is no longer dispersive due to the even power terms in the expansion. We thus require this term to be suppressed compared to the term due to polarization rotation:

$$\frac{|T_y(1 - 2b_y) - T_x(1 - 2b_x)|}{8} \tan 2\beta \frac{\Delta\nu}{\nu_0 - \nu} \ll \frac{T_x(1 - 2b_x) + T_y(1 - 2b_y)}{2} \sqrt{1 - \left(\frac{T_y(1 - 2b_y) - T_x(1 - 2b_x)}{\cos 2\beta (T_x(1 - 2b_x) + T_y(1 - 2b_y))} \right)^2} \quad (\text{Eq. S18})$$

In addition, the relative amplitude \mathcal{A} of the polarization rotation signal

$$\mathcal{A} = e^{-\sigma n l} \cos 2\beta \frac{T_x(1 - 2b_x) + T_y(1 - 2b_y)}{2} \times \sqrt{1 - \left(\frac{T_y(1 - 2b_y) - T_x(1 - 2b_x)}{\cos 2\beta (T_x(1 - 2b_x) + T_y(1 - 2b_y))} \right)^2} \quad (\text{Eq. S19})$$

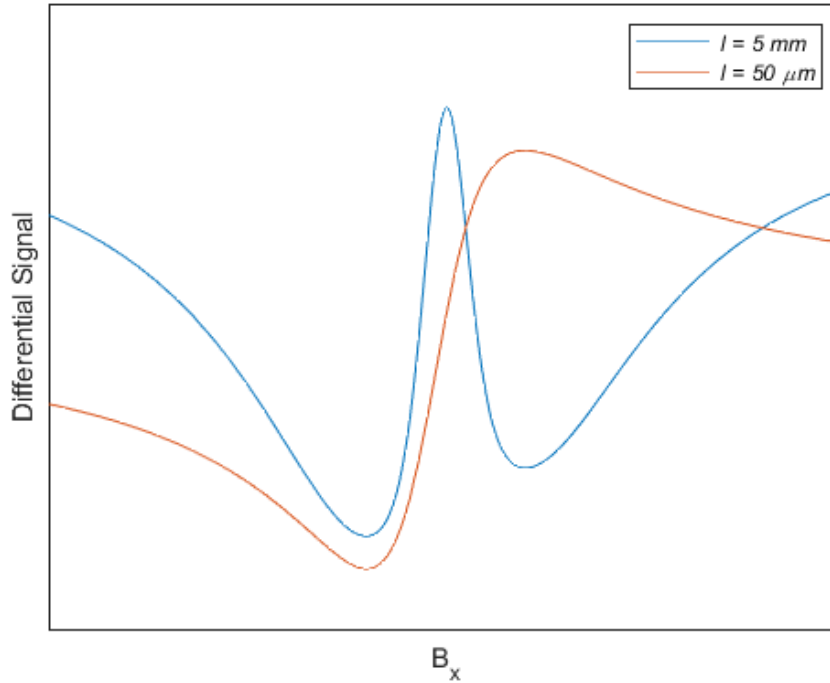


FIG. S1. Simulated differential signal \mathcal{D} due to circular dichroism for a vapor cell with optical path length of 5 mm (blue) and 50 μm (red). The figure is not to scale and only shows the overall shape of the signal.

should be maximized once (Eq. S18) is satisfied.

Using the laser detuning, ellipticity, and linewidth specified in [1], we rewrite the condition in (Eq. S18) in terms of the figure of merit introduced in Section 3 of the main text:

$$FOM = \left| \frac{T_y(1 - 2b_y) - T_x(1 - 2b_x)}{T_x(1 - 2b_x) + T_y(1 - 2b_y)} \right| \ll 0.707 \quad (\text{Eq. S20})$$

Considering that the FOM is bounded to ≤ 1 , we therefore see that (Eq. S18) can be easily satisfied. In addition, the signal can be further optimized by choosing a different ellipticity β and detuning $\nu_0 - \nu$. For a sufficiently small vapor cell such that $\Lambda = n\sigma l P_z \ll 1$, (Eq. S18) is no longer required, and we can instead maximize the signal in the linear P_z regime:

$$\mathcal{D} = \xi E_0^2 e^{-\sigma n l} \cos 2\beta \sin \phi \quad (\text{Eq. S21})$$

References for the Supplementary Information

1. V. Shah and M. V. Romalis, "Spin-exchange relaxation-free magnetometry using elliptically polarized light," *Phys. Rev. A* **80**(1), 013416 (2009).